A Mixed-Layer Model of the Diurnal Dryline

PATRICK A. JONES AND PETER R. BANNON

Department of Meteorology, The Pennsylvania State University, University Park, Pennsylvania

(Manuscript received 13 August 2001, in final form 27 February 2002)

ABSTRACT

This study examines the diurnal behavior of the dryline system using a mixed-layer model to represent the cool moist air capped by an inversion to the east of the line. This inversion is referred to as the dry front, and the intersection of this dry front with the terrain is the dryline. The results indicate that boundary layer heating is sufficient to drive the dryline and explain its diurnal variation.

The daytime eastward propagation of the model dryline of 200 km agrees well with other numerical studies and is in approximate agreement with dryline observations. The present model results also indicate a nearly vertical inversion slope up to a height of 2 km in the early afternoon. Model simulations with sloping terrain consistently yield a nocturnal low-level jet between 0000 local time (LT) and 0100 LT, with a speed of 20–25 m s^{-1}, located below the inversion.

The effect of each mixed-layer process, such as entrainment, surface heat flux, and nighttime cooling, is examined. Entrainment tends to steepen the slope of the dry front near the dryline but has little impact on its eastward advance. The dryline advance is most sensitive to the amplitude of the surface heat flux relative to the depth of the mixed layer and the strength of the inversion. Large heat fluxes, in combination with a shallow mixed layer and a weak inversion, produce the greatest dryline advance. The westward surge of the dryline at dusk is most sensitive to the amplitude of the nighttime cooling: larger cooling produces a larger surge.

The model simulations consistently predict a local maximum in the inversion height (called a spike) near the dryline at dusk associated with entrainment and boundary layer convergence. This process may be one of the possible triggers for the deep convection often seen just to the east of the dryline.

1. Introduction

The south-central plains of the United States is often the site for the development of a surface boundary between dry and moist air masses known as the dryline. The dry air mass generally originates in the desert southwest, while the moist air mass originates from the Gulf of Mexico. The occurrence of severe weather in the plains during the spring and summer months is often linked to the presence of the dryline. Schaefer (1986), and more recently Miller et al. (2001), provide overviews of the observations and theories of the dryline, as well as bibliographies of the literature. The moist air is capped by an inversion. We refer to this airmass boundary as the dry front, and its intersection with the sloping terrain as the dryline.

The diurnal behavior of the dryline is characterized by a daytime eastward movement, and a nighttime westward retrogression. The slope of the dry front steepens during the day and relaxes at night. Conversely, the surface winds in the moist air are a maximum near midnight and weaken during the day.

The purpose of the present study is to model this diurnal variation of the dryline using a mixed-layer model. The shallow moist air mass to the east of the dryline is treated as a mixed layer convectively driven by surface buoyancy fluxes. The moist air is overlaid by an elevated mixed layer (e.g., Lanicci and Warner 1991) of uniform potential temperature that is decoupled from the surface. The difference in potential temperature between the two layers manifests itself as an inversion or ''lid'' that inhibits the development of deep convection over the plains. The present investigation is an extension and refinement of the shallow-water modeling study by Miller et al. (2001) who prescribe the diurnal variation of the entrainment and the inversion strength. In the present study, we predict these quantities using standard mixed-layer theory (e.g., Tennekes 1973; Stull 1988).

The next section presents the mixed-layer model of the moist air mass. The standard model equations are solved numerically using the technique of Schär and Smolarkiewicz (1996) that can handle vanishingly small layer depths. Section 3 presents the results of numerical experiments that isolate the effects of entrainment, surface heating, nighttime cooling, and topography.

2. The model

Figure 1 illustrates the geometry and physics of the model dryline system on an f plane. The x axis is normal

Corresponding author address: Peter R. Bannon, Dept. of Meteorology, The Pennsylvania State University, University Park, PA 16802.
E-mail: bannon@ems.psu.edu

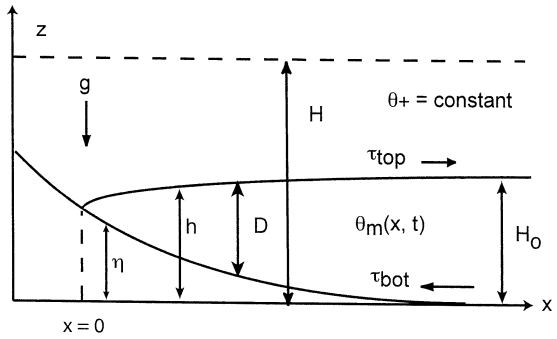

FIG. 1. Schematic diagram of the mixed-layer model physics of the dryline system on an f plane. The cool moist mixed layer of depth D and potential temperature θ_m lies between the sloping bottom topography η and an elevated mixed layer of warm dry air with potential temperature θ_+. An inversion of strength $\Delta\theta = \theta_+ - \theta_m$ lies at the height h. The intersection of this inversion (or dry front) with the ground denotes the location of the dryline. Southerly flow in the form of a low-level jet exists in the cool moist air. The stress on the top layer is indicated by the arrow labeled τ_{top}. The stress on the bottom layer is indicated by the arrow labeled τ_{bot}.

and the y axis is parallel to the dryline. Henceforth we refer to these as the eastward and northward directions respectively. The z axis is in the vertical. The u and v winds are parallel to the x and y axes, respectively. The dryline model is assumed to be one-dimensional with variations only in the x direction.

The height of the inversion is denoted by h, the variable terrain height by η, and the fluid depth by $D = h - \eta$. Far to the east the terrain is flat and the inversion height and fluid depth approach the value $H_0 = 2$ km. The terrain η is either flat or is given by an exponential of the form (Kovacs 1996)

$$\eta = \eta_0 e^{-x/b}, \tag{1}$$

where $\eta_0 = 2$ km, $b = 450$ km, and $x = 0$ is the location of the dryline (i.e., $D = 0$) at the initial time ($t = 0$). These choices for η enable analytic initial conditions (see section 2c).

The thermal structure of the dryline system is described by the vertically uniform potential temperature $\theta_m(x, t)$ of the mixed layer that is overlaid by an elevated mixed layer of uniform potential temperature θ_+. The strength of the inversion is

$$\Delta\theta \equiv \theta_+ - \theta_m. \tag{2}$$

We assume the elevated mixed layer is infinitely deep and time-independent. The mixed layer is in contact with the surface and undergoes a strong diurnal cycle of heating during the day and cooling at night. The daytime heating produces convective activity that can entrain elevated mixed-layer air across the inversion and into the mixed layer. The use of a mixed-layer model is not without some limitations. Its use precludes an examination of the detailed structure of the nonhydrostatic behavior of the leading edge of the dryline or of the secondary internal circulations within the moist air.

a. Mixed-layer equations

The continuity and momentum equations are, respectively,

$$\frac{DD}{Dt} = D\nabla \cdot \mathbf{u} + w_e, \tag{3}$$

$$\frac{D\mathbf{u}}{Dt} + f\hat{\mathbf{z}} \times \mathbf{u} = -\overline{\frac{1}{\rho_o}\nabla p} + \left(\frac{\boldsymbol{\tau}_{top} - \boldsymbol{\tau}_{bot}}{\rho_0 D}\right), \tag{4}$$

where $D/Dt = \partial/\partial t + u\partial/\partial x$, $\mathbf{u} = (u, v)$ is the horizontal velocity, $f = 1 \times 10^{-4}$ s^{-1} is the constant Coriolis parameter, $\boldsymbol{\tau}_{top}$ is the stress on the top layer, $\boldsymbol{\tau}_{bot}$ is the stress on the bottom layer, ρ_0 is a constant reference density, and w_e is the entrainment rate (Tennekes 1973) that represents the rate at which elevated mixed-layer air is carried across the inversion into the mixed layer.

The quadratic form of surface friction is, following Miller et al. (2001),

$$\boldsymbol{\tau}_{bot} = \rho_0 C_d |\mathbf{u}| \mathbf{u}, \tag{5}$$

where C_d is the dimensionless drag coefficient. Though C_d depends on the surface roughness and the atmospheric stability near the surface, it is taken to be spatially uniform in our experiments. We assume that the turbulent vertical transport of momentum is convectively driven by the surface heat flux. Then the daily cycle of surface friction is incorporated into the model by using a time-dependent drag coefficient C_d of the form

$$C_d(t) = \begin{cases} 2 \times 10^{-3}\left[1 - \cos\dfrac{\pi t}{10h}\right] & \text{from 0600 to 1800 LT} \\ 0 & \text{otherwise.} \end{cases} \tag{6}$$

This choice yields a surface friction that increases from zero at sunrise [0600 local time (LT), $t = 0$] to a late afternoon maximum at 1600 LT, and then instantly drops to zero at sunset (1800 LT), as in Blackadar (1957). Miller et al. (2001) plot (6) in their Fig. 5.

The stress on the top layer $\boldsymbol{\tau}_{top}$ represents the addition of momentum as air aloft is entrained into the dry front. This process is expressed by the equation

$$\boldsymbol{\tau}_{top} = \rho_0 w_e(\mathbf{u}_{top} - \mathbf{u}), \tag{7}$$

where $w_e > 0$ is the entrainment of warm dry air across the dry front during the day, and $\mathbf{u}_{top}$ is the prescribed horizontal velocity of the air aloft. Because the model only describes the dynamics of the cool moist air, the process of momentum mixing can only be incorporated to the east side of the dry front. Thus, our test of the theory of McCarthy and Koch (1982) that the movement of the dryline is associated with momentum mixing from aloft is only a partial one.

The momentum equation (4) contains a depth-aver-

aged pressure gradient term of the form (e.g., Keyser and Anthes 1977)

$$-\overline{\frac{1}{\rho_0}\nabla p} = \left[-\frac{g\Delta\theta}{\theta_0}\frac{\partial h}{\partial x} + \frac{gD}{2\theta_0}\frac{\partial \theta_m}{\partial x} - \frac{1}{\rho_0}\frac{\partial p'(H)}{\partial x}\right]\hat{\mathbf{x}}, \quad (8)$$

where $\theta_0 = 300$ K is the reference potential temperature in the Boussinesq approximation and $g = 10$ m s^{-2} is the acceleration due to gravity. Here H is a reference height for the pressure (see Fig. 1) and is arbitrary provided it exceeds h. The result (8) holds rigorously for a two-layer Boussinesq fluid in hydrostatic balance. This expression takes proper account of the thermal structure that can exist both inside and above the mixed layer. The first term in (8) is analogous to the reduced gravity term in Miller et al. (2001). The second term is the pressure gradient force due to horizontal variations in the mixed-layer potential temperature. The third term in (8) is the synoptic-scale pressure gradient that can drive motion in the mixed layer. We take this term to be a zonal pressure gradient force that drives a uniform 8 m s^{-1} geostrophic v field. This assumption relieves the h and θ_m fields from the burden of driving the mean low-level winds. Such winds are believed to be present for the development of the low-level jet (Blackadar 1957). We assess the impact of this synoptic-scale pressure gradient in section 3e.

The thermodynamic evolution of the mixed layer is described (Tennekes 1973) by

$$\frac{D\theta_m}{Dt} = \frac{\overline{(w'\theta')}_{\text{surface}} - \overline{(w'\theta')}_{\text{inversion}}}{D} + \dot{\theta}_{\text{rad}}, \quad (9)$$

where $\overline{(w'\theta')}_{\text{surface}}$ is the heat flux off the surface and the downward heat flux across the inversion $\overline{(w'\theta')}_{\text{inversion}}$ is related to the entrainment rate w_e by

$$\overline{(w'\theta')}_{\text{inversion}} = -w_e\Delta\theta. \quad (10)$$

The last term in (9) describes nocturnal radiative cooling.

Closure of the mixed-layer model requires a relation between the surface flux and the inversion flux. Zeman and Tennekes (1977) argue that the appropriate closure for a mixed layer overlaid by an adiabatic fluid is

$$\overline{(w'\theta')}_{\text{inversion}} = -\left[\frac{C_F}{1 + C_T w_*^2\theta_0/gD\Delta\theta}\right]\overline{(w'\theta')}_{\text{surface}} \le 0, \quad (11)$$

where the convective velocity scale w_* is defined by

$$w_*^3 \equiv \frac{gD}{\theta_0}\,\overline{(w'\theta')}_{\text{surface}}. \quad (12)$$

Here, the constants are $C_T = 3.55$ (Zeman and Tennekes 1977) and $C_F = 0.20$ (Tennekes 1973). The expression (11) is a better physical representation than the simple proportionality of Tennekes (1973) that uses (11) with $C_T = 0$, for it inherently contains a horizontal dependence through D and $\Delta\theta$.

The surface heat flux is a diurnally varying quantity, and this model uses a sinusoidally prescribed variation for it. The peak is at 1300 LT (where 0600 LT is sunrise) and goes to zero just after sunset (1800 LT), at which time a constant radiative nighttime cooling takes effect. We are then simply taking the positive part of a sine curve. Mathematically we write

$$\overline{(w'\theta')}_{\text{surface}} = \begin{cases} \overline{(w'\theta')}_0 \sin\left(\dfrac{\pi t}{t_{\max}}\right), & 0600 \text{ LT} \le t \le 1800 \text{ LT} \\ 0, & \text{otherwise,} \end{cases} \quad (13)$$

where $t_{\max}$ determines when the heat flux is a maximum. This maximum typically lags the maximum insolation (Stull 1988) and here we take $t_{\max} = 13$ h. The value of the radiative cooling $\theta_{\text{rad}} = -0.330$ K h^{-1} is approximately that needed to restore the inversion strength overnight. With the surface heat flux prescribed by (13), the inversion heat flux is diagnosed using (11) and the entrainment rate is then found from (10).

b. Model numerics

The governing equations are solved using finite differencing with the conservative flux form as described in Schär and Smolarkiewicz (1996). Their first-order differencing algorithm includes a flux correction formalism that reduces the computational diffusion and makes it possible to handle the case where the depth of the dry front goes to zero. The rotational and frictional terms are coded using classical implicit numerics, specifically a trapezoidal finite-differencing scheme. The pressure gradient term follows the work of Smolarkiewicz and Margolin (1993). The friction and Coriolis terms are coded using an implicit finite-differencing scheme. The model uses a staggered grid, having h, $\Delta\theta$, and v specified on the same gridpoint with u specified a half grid length to the east. The grid resolution is 2.5 km. The model domain is 2×10^3 km. The time step, 20 s, satisfies the Courant–Friedrichs–Lewy (CFL) criterion.

Miller (1998) presents the results of a simple control run to verify the numerics for a shallow-water version of our model. The current mixed-layer model is tested by verifying that the far field ($D \approx H_0$) behavior of the dryline obeys strictly mixed-layer physics because the advective dynamical effects are negligible there. In particular a horizontally homogeneous form of the model accurately reproduces the solutions in Tennekes (1973) and Zeman and Tennekes (1977).

c. Initial and boundary conditions

The initial conditions of the model are an f-plane version of the Wexler (1961) model of the climatological

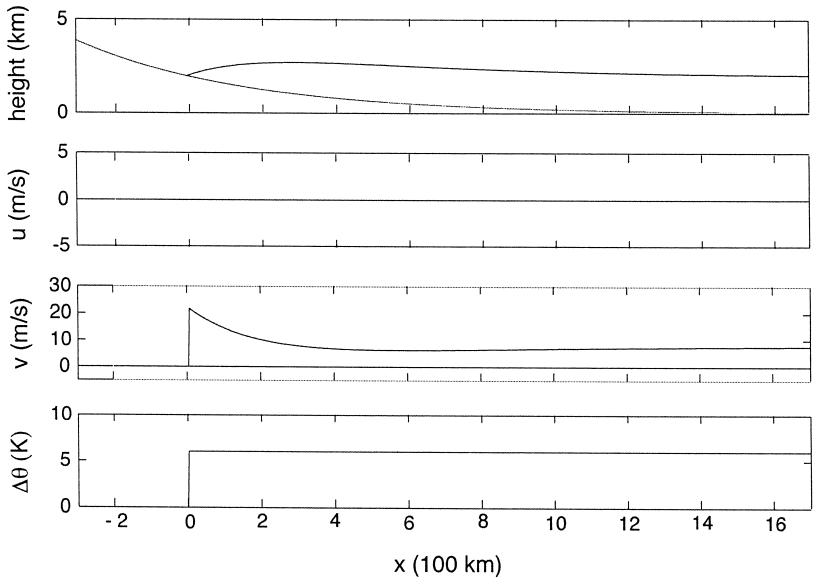

FIG. 2. The model initial conditions with topography. The fields are plotted as a function of distance x from the dryline ($x = 0$).

mean southerly jet in geostrophic balance. The mixed-layer equations have an exact nonlinear, uniform potential vorticity, steady-state solution without friction ($\tau = 0$) and without entrainment ($w_e = 0$). Kovacs (1996) provides the solution with an exponential topography (1) similar to that of the Great Plains. The initial conditions used here are identical to those in Miller et al. (2001) except for the addition of a uniform 8 m s^{-1} meridional wind. The case without terrain appears in their Fig. 4; the case with terrain is displayed in Fig. 2. This solution holds only for the case of an elevated mixed layer aloft that has no variation in potential temperature.

The initial conditions for h and v exhibit a low-level jet with a maximum of 23 m s^{-1} at the western edge of the dryline system where $D = 0$. There is no initial u velocity. The maximum depth of the mixed layer is 2 km. These conditions are assumed to reflect a mean dryline system valid at dawn (0600 LT). The v field decays exponentially with distance from the dryline and approaches a uniform speed of 8 m s^{-1} in the far field. The inversion strength is a uniform 6 K.

The eastern boundary in the x direction is open such that the normal gradient of each variable is set to zero. Test results proved that this condition is acceptable because there is little reflection at the boundary. The western edge of the fluid where D and θ_m vanish is treated following Schär and Smolarkiewicz (1996). This scheme uses an upstream differencing of the advective terms in flux form that keeps the fluid depth D and mixed-layer potential temperature θ_m nonnegative with a flux correction to reverse the effects of the computational diffusion. Momentum averaging, rather than velocity averaging (Schär and Smith 1993) is used to keep the velocity fields bounded in regions where the depth of the fluid is vanishing. Tests of the algorithm (Schär and Smolarkiewicz 1996; Miller 1998) indicate that the scheme can accurately handle both advancing and retreating layers of fluid.

3. Results

In order to assess the effects of model physics on the simulation of the dryline, we first present the results of a benchmark experiment in section 3a. Section 3b assesses the effects of the choice of the inversion heat flux parameterization. Section 3c examines the role of topography on the model dryline and documents the evening westward surge of the dryline in detail. Section 3d examines the effect of the strength of the prescribed surface heat flux and nocturnal cooling on the model dryline. Section 3e addresses the role of the pressure gradient force (8) on the flow. Section 3f considers the role of the prescribed far field height H_0. In each experiment, the initial model time $t = 0$ corresponds to 0600 LT. Each section presents the results of 1-day simulations except section 3g that presents the results of a 3-day model simulation.

The dryline movement is measured using the zero fluid depth contour ($D = 0$). All model runs include the surface friction given by (5) and (6). As in Miller et al. (2001), the effect of such a drag by itself is to produce a westward-moving dryline during the day that is inconsistent with observations. In addition, the momentum mixing term (7) has no discernible impact on the dryline simulations (results not shown) and is not included in the model runs presented here. Miller et al. (2001) found similar results.

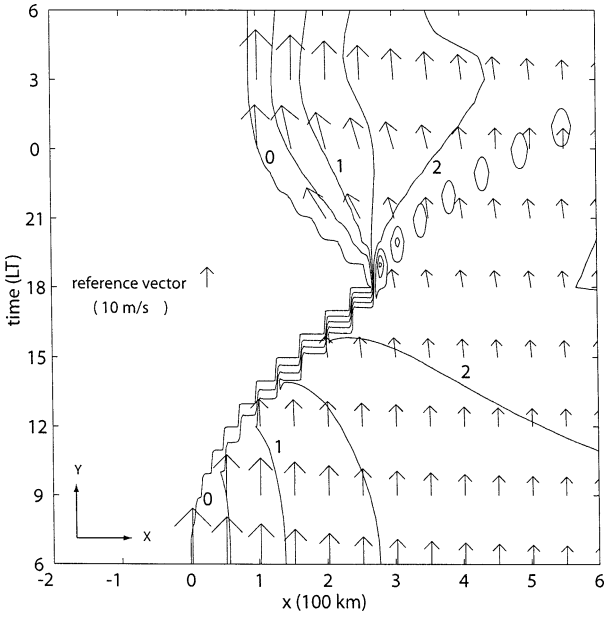

FIG. 3. Contour plot of mixed-layer depth D in x–t space with wind vectors (u, v) in x–y space for the case with no topography, a surface heating amplitude of $\overline{(w'\theta')}_0 = 0.30$ K m s^{-1}, and a nocturnal radiative cooling rate of 0.330 K h^{-1}. In this and subsequent contour plots, the depth contour interval is 0.5 km, selected contours are labeled in km, and the reference vector is 10 m s^{-1}.

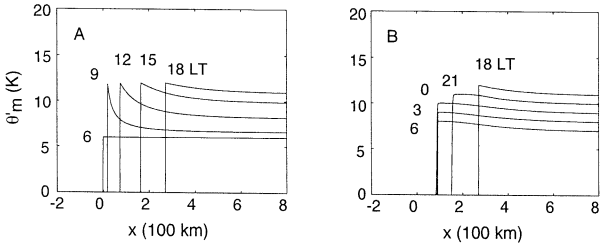

FIG. 4. Perturbation mixed-layer potential temperature $\theta'_m = \theta_m - \theta_0$ for the case of Fig. 3 as a function of horizontal distance x, at 3-h intervals (labeled in LT) for (a) daytime and (b) nighttime. For reference the perturbation elevated-mixed-layer potential temperature is $\theta'_+ = \theta_+ - \theta_0 = 12$ K and is constant in time and the inversion strength $\Delta\theta = \theta'_+ - \theta'_m$.

a. Benchmark experiment

As a standard for comparison we first present results for an integration without terrain ($\eta = 0$). The initial parameter settings are an inversion strength $\Delta\theta$ of 6 K, a far field mixed-layer depth H_0 of 2 km. The diurnal variation is driven by the prescribed surface heat flux (13) with an amplitude of 0.30 K m s^{-1}. The closure assumption for the inversion flux is (11) with $C_F = 0.20$ and $C_T = 3.55$.

Figures 3 and 4 present the results for a 1-day simulation. During the day, the dryline moves approximately 280 km to the east of its initial position, followed by a nighttime retrogression of 200 km. The wind field, shown with arrows, has pronounced extrema, with a u-field maximum around 2 m s^{-1} westward, and v-field minimum of 8.4 m s^{-1} at the dryline at 1800 LT. At night, the u field reaches a maximum of 11 m s^{-1} by 2000 LT, while the v field increases to approximately 26 m s^{-1} around 0400 LT.

The ''stair-step'' nature of the dry front depth contours displayed in Fig. 3 and elsewhere is a consequence of the steep slope of the dry front when entrainment acts to eliminate the line and of the fact that the fields are sampled at 1-h intervals. No smoothing has been performed on any of the fields.

During the day, the inversion height rises due to entrainment; dynamical considerations seem relatively minor. At dusk (1800 LT) the westward surge of the dryline commences and produces a rapid decrease in the slope of the dry front to the east. Also at dusk there is a sharp spike in the height of the mixed layer of about 1500 m, indicative of enhanced convergence. As a result of this spike, an isolated wave of increased inversion height propagates to the east. The features of this surge and spike are examined in more detail in section 3c for the more realistic case that includes topography.

The thermodynamic fields (Fig. 4) exhibit a large diurnal variation. Here we plot the perturbation mixed-layer potential temperature $\theta'_m = \theta_m - \theta_0$. For reference, the perturbation elevated-mixed-layer potential temperature is $\theta'_+ = \theta_+ - \theta_0 = 12$ K and is constant in time. Initially $\theta'_m = 6$ K. When $\theta'_m > \theta'_+$, we set θ'_m and D to zero to indicate the edge of the cool moist air mass. During the day the mixed layer is warmed most rapidly near the dryline where the mixed-layer depth is shallowest. Even far from the dryline the inversion strength has been reduced to a minimum inversion $\Delta\theta$ of 1 K by sunset. A strengthening back to 5 K occurs at night, due to the prescribed radiative cooling. The effect of this cooling is studied in section 3d.

An important feature of the θ_m field is that its gradient is always directed westward toward the dryline. This feature is consistent with daytime observations (e.g., Ziegler and Hane 1993). The gradient is strongest during the midmorning and weakest at night.

b. Heat flux ratio parameterization

In order to assess the role of the closure assumption (11) on the benchmark simulation, two additional model runs were performed (results not shown). In the first the variable closure (11) is replaced with the constant heat flux ratio closure of Tennekes (1973) by setting $C_T = 0$. This case is qualitatively similar to the variable ratio case in every respect. Quantitative differences due to the slightly larger entrainment rate include a higher far field inversion height, a larger spike at dusk, and a slightly greater (by 25 km) westward surge at night. The maxima and minima behave as in the previous case. We conclude that the C_T term in (11) has no significant qualitative impact on the model dryline.

A second experiment considered the case of encroachment, for which the inversion heat flux (11) is

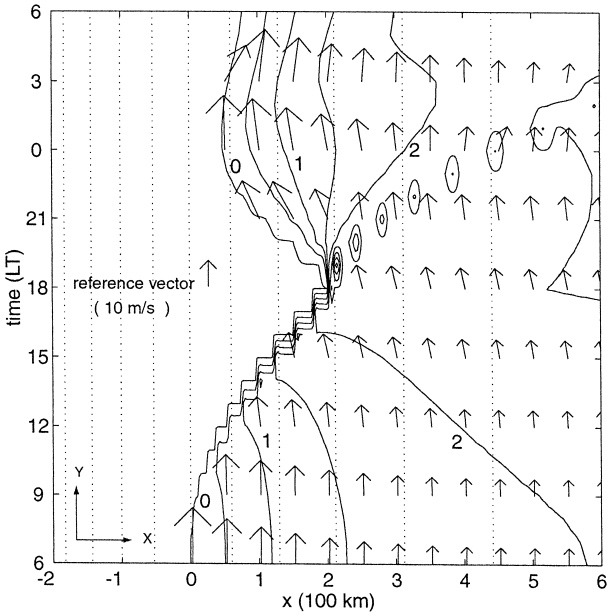

FIG. 5. Contour plot of mixed-layer depth D with wind vectors for the case of Fig. 3 but with topography (1). In this and subsequent contour plots with topography, the dotted lines indicate topography with a contour interval of 0.25 km, and the 2-km contour is aligned with $x = 0$.

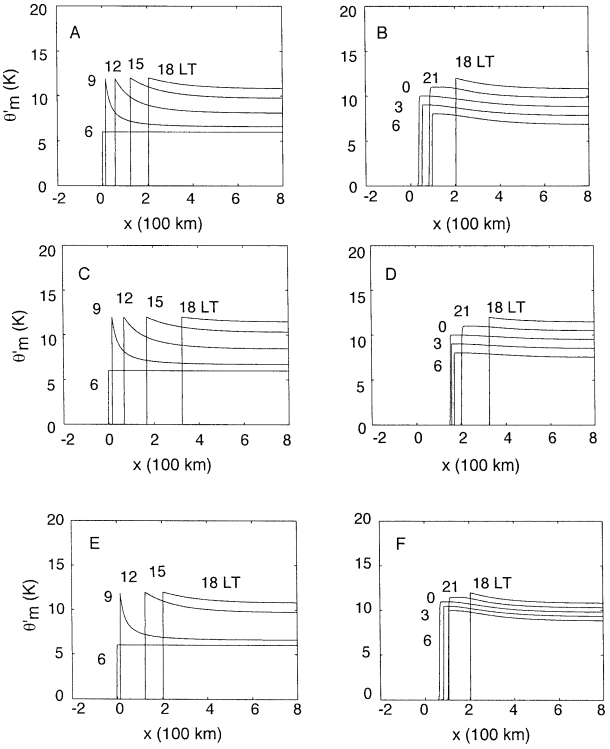

FIG. 6. Perturbation mixed-layer potential temperature $\theta'_m = \theta_m - \theta_0$. as a function of horizontal distance x, at 3-h intervals (labeled in LT) for (left) daytime and (right) nighttime. (a), (b) For the case of Fig. 5; (c), (d) for the case of Fig. 8, whose surface heating amplitude is $\overline{(w'\theta')}_0 = 0.35$ K m s^{-1}; (e), (f) for the case of Fig. 9, whose nocturnal radiative cooling rate is 0.165 K h^{-1}.

set to zero ($C_F = 0$). Again, the results (not shown) reveal little sensitivity to the change in the closure assumption. For example, here the dryline moves eastward about 50 km less than the result shown in Fig. 3 during the day. The major difference is that the inversion height to the east of the dryline remains unchanged because there is no entrainment and thus no mechanism for changing the inversion height. This result lends support to our interpretation in section 3b that the inversion height is primarily controlled by the thermodynamics during the daytime. A spike of 500 m develops just after dusk but it is much weaker than that for the cases with entrainment. Thus, entrainment is an important process in the development of a strong spike.

c. *Effect of bottom topography*

Next, we consider the addition of sloping terrain of the form (1). The results (Fig. 5) show an eastward movement of the dryline of 205 km during the day. The u-field maximum at 1800 LT is 2.4 m s^{-1} westward, while the v field decreases to 9 m s^{-1} northward by this time. After sunset, the dryline surges westward by 145 km, with the u field increasing to 9 m s^{-1} at 2000 LT. The v-field maximum at 0200 LT of 22 m s^{-1} is in accord with a nocturnal jet (e.g., Bonner 1968). The mixed-layer potential temperature in this case (Figs. 6a,b) displays a variation nearly identical to that in Fig. 4. Figures 6c–f are for different cases, which will be discussed later. There is a decrease in the far field inversion strength to 1.2 K by sunset, while the nighttime cooling increases its strength to 5.1 K by sunrise.

Despite the similarity between this and the benchmark run, there are clear differences. In particular, the daytime movement is 75 km less compared with that of the no-terrain case. We attribute this behavior to the fact that the initial depth D of the dry front is greater for the terrain case. Here the initial depth is constrained by the assumption of uniform potential vorticity (Kovacs 1996) to have the form

$$D(x) = H_0\left[(1 - e^{-x/R}) + \frac{\eta_0}{H_0}\frac{R^2}{b^2 - R^2}(e^{-x/b} - e^{-x/R})\right], \tag{14}$$

where b and η_0 are defined by the terrain (1), H_0 is the far field depth, and $R = (g'H_0/f_0^2)^{1/2} = 200$ km is the Rossby radius. The second term in (14) is the additional depth present with terrain. Because this quantity is positive ($b > R$), there is a greater volume of air to be eliminated as the dryline advances eastward in the terrain case.

In addition the nighttime surge in the terrain case is 25 km less than the no-terrain case. This behavior is consistent with having the term $-g'\partial\eta/\partial x > 0$ in the

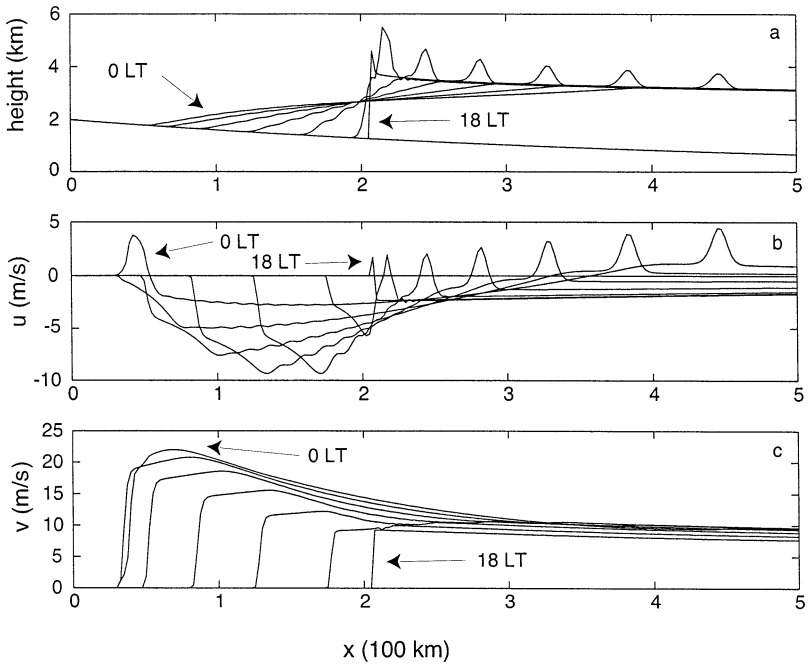

FIG. 7. Cross sections of the dynamic fields for the 6 h after sunset in the case of Fig. 5. The dryline stops at 0000 LT and moves eastward thereafter.

pressure gradient force. At night the flow is uphill and moves in opposition to gravity, and so there is a loss of kinetic energy relative to the no-terrain case. The westward surge in the terrain case ceases by midnight and there is the start of an eastward advance of the dryline before dawn. This feature is absent in the no-terrain case.

Figure 7 shows a detailed view of the nighttime surge for this case at sunset and the first 6 h thereafter. The spike in the inversion height extends 1 km above the mean inversion height at 1800 LT. By 1900 LT it extends over 2 km. This increase occurs after the surface heating (13) has terminated, and thus, it is the result of boundary layer convergence rather than entrainment. The spike initially weakens as it propagates eastward. This isolated wave of increased inversion height is associated with a pulse of eastward winds that propagates to the east. This feature is reminiscent of pressure jump lines (Tepper 1955) but here it is a relatively weak linear phenomenon generated at dusk with the cessation of the daytime heating and the commencement of the nighttime cooling. To the west one can clearly see the surge slow down approaching midnight just before the slight eastward movement starts again (see Fig. 5).

Figures 7a and 6b indicate that a representative fluid depth and inversion strength at 1800 LT are 2 km and 1 K, respectively. The corresponding gravity wave phase speed $c_g = (g\Delta\theta D/\theta_0)^{1/2}$ is 8.2 m s^{-1}. This value is consistent with the surge speed around 1900 LT. The subsequent acceleration of the surge is due to the influence of the synoptic pressure gradient force and the increase in the inversion strength associated with the radiative cooling. The speed is always less than the speed (2 c_g) associated with the nonrotating dam break problem (see Miller et al. 2001).

Examination of Fig. 7 shows that the slowing of the westward surge is consistent with a northward deflection of the westward flow by the Coriolis force. Just before the surge stops its westward movement, the inversion slope has become considerably gentler than when it started out at sunset (see Fig. 7a). This deceleration happens very quickly; the surge speed decreases by over 10 m s^{-1} in just 3 h.

Visual inspection of Fig. 7 suggests that the wind field curves extend farther to the east than the western edge of the depth of the mixed layer. The model output (not shown) indicates that the depth and wind fields are consistent but that the mixed-layer depths can be exceedingly small. For example the depth D is no greater than 3 m in the vicinity of the eastward peak in the zonal wind field at the leading edge of the dryline at 0000 LT.

d. Heating–cooling cycle

The surface heat flux is the primary physical process driving the mixed-layer physics. In Fig. 8, we have increased the heat flux amplitude to 0.35 K m s^{-1}, slightly larger than the 0.30 K m s^{-1} used previously. The daytime movement is 325 km eastward, with u and v values of 2 m s^{-1} and 8.4 m s^{-1}, respectively, by sunset at the dryline. The westward surge is 160 km with a maximum u of 9 m s^{-1} west at 2100 LT. The behavior of both fields is essentially identical to previous cases. The ther-

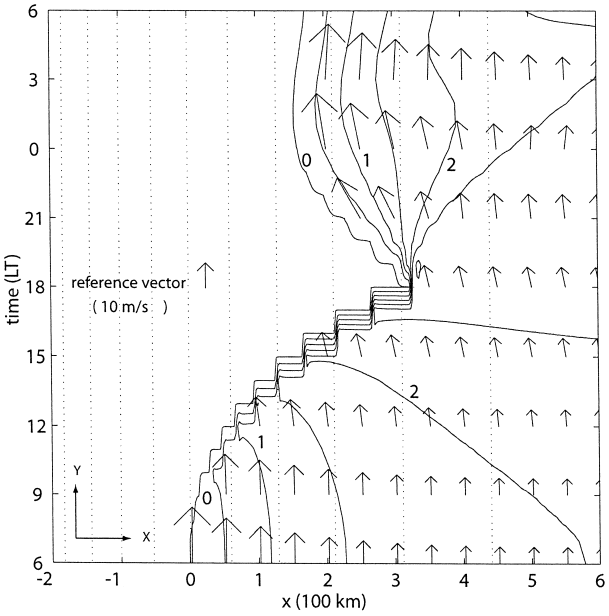

FIG. 8. Contour plot of mixed-layer depth D with wind vectors for the case similar to Fig. 5, but with a surface heating amplitude of $\overline{(w'\theta')}_0 = 0.35$ K m s^{-1}.

modynamic variables (Figs. 6c,d) act in accordance with the increased heat flux. The far field inversion strength (not shown) decreases to 0.5 K by sunset, less than half the value found for any of the lesser heat flux simulations. The maximum θ_m is greater by 0.65 K, which is consistent with (9) (i.e., a greater flux leads to a higher rate of change of θ_m).

One primary difference between this and the other cases is the eastward movement: an increase of only 0.05 K m s^{-1} in the flux amplitude yields a 100-km greater displacement. This behavior is not surprising since the inversion heat flux is larger and $\Delta\theta$ decreases faster, leading to increased entrainment of upper-layer air into the lower layer, and so faster elimination of the inversion.

A second difference is that this case exhibits neither a significant spike in the inversion height at dusk nor a downstream wave. We attribute their absence here to the fact that the larger heating produces a uniform mixed-layer temperature by dusk (not shown). Thus the second term in the pressure gradient force (8) related to the variation in mixed layer temperature is relatively insignificant. This issue is examined further in the next section, which deals with the influence of the pressure gradient force.

Table 1 summarizes a series of simulations on the effect of the amplitude of the daytime surface heat flux. As expected, the inversion strength at 1800 LT increases with decreasing heat flux while the eastward advance decreases. Overall, the westward retreat decreases slightly with decreasing heat flux. The strength of the low-level jet is relatively insensitive to the heat flux amplitude.

TABLE 1. The effect of the amplitude of the surface heat flux $(\overline{w'\theta'})_0$ on the far field inversion strength at 1800 LT $\Delta\theta$, eastward advance x_{max}, and westward retreat Δx of the dryline and the strength of the low-level jet v_{max}.

$(\overline{w'\theta'})_0$ (K m s^{-1})	$\Delta\theta$ (K)	x_{max} (km)	Δx (km)	v_{max} (m s^{-1})
0.35	0.5	325	160	22
0.30	1.5	205	145	22
0.25	2.0	128	133	21
0.20	2.5	78	128	20
0.15	3.5	35	140	20

Just as the surface heat flux is crucial in moving the dryline eastward during the day, the radiative cooling at night is important in its westward retrogression. Figure 9 shows the results of decreasing the cooling to -0.165 K h^{-1}, or one-half the value it has had up to this point. Comparison of Figs. 9 and 5, and of Figs. 6a and 6b, shows that the daytime integrations are identical, as they should be. The present nighttime integration displays 50 km less movement than that in Fig. 5. This behavior seems contradictory to intuition, since a cooling reduction would seem to imply a reduction in the tendency to move downslope. However, the cooling also impacts the movement by altering the pressure gradient (8) via $\Delta\theta$, and this counteracts any tendency the flow might have to move downslope.

The nighttime u-field maximum is 7 m s^{-1} westward and occurs at 2100 LT before veering eastward toward dawn. The v field becomes a minimum at 2100 LT decreasing to 10 m s^{-1} before reaching a 20 m s^{-1} maximum northward shortly after midnight. The thermo-

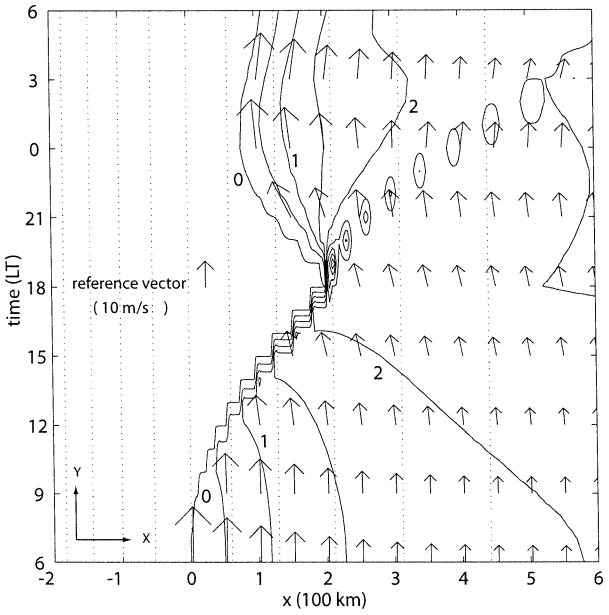

FIG. 9. Contour plot of mixed-layer depth D with wind vectors for the case similar to Fig. 5, but with a nocturnal radiative cooling rate of 0.165 K h^{-1}.

dynamic fields (Figs. 6e,f) behave in exact accordance with the decreased cooling rate. In particular, the nighttime increase of $\Delta\theta$ to 3.2 K is just half of the corresponding change seen in Fig. 6b.

The heating–cooling cycle as described here then plays an important part in adjusting the pressure gradient, so that the nighttime retrogression is not overpredicted. The observation of less westward movement with lower cooling is now more understandable, considering how the lower cooling reduces the pressure gradient to the west.

At the suggestion of a reviewer, we tested the role of a downward heat flux at night. A model run identical to that displayed in Fig. 7, but with the inclusion of a small downward heat flux of 0.05 K m s^{-1}, produced an unrealistically large inversion strength of several tens of Kelvins at the leading edge of the surge. The reason for this behavior is that the warming rate of the mixed layer is given by the surface heat flux divided by the mixed-layer depth *D*. The prescribed downward flux produces unrealistic cooling rates where the depths are extremely shallow.

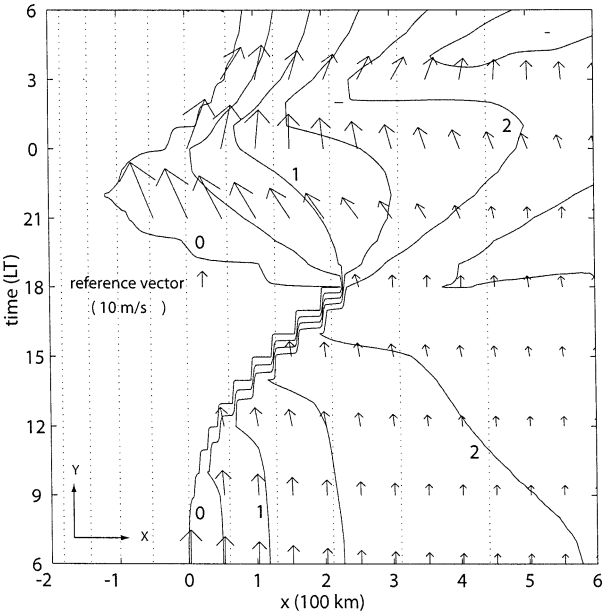

FIG. 10. Contour plot of mixed-layer depth *D* with wind vectors for the case similar to Fig. 5, but with constant mixed-layer strength imposed in the pressure gradient force (8) only. The synoptic forcing is also removed.

e. Pressure gradient considerations

We next consider the interaction between the thermodynamics and the dynamics. The thermodynamics will alter the strength of the inversion $\Delta\theta$ and this in turn will modulate the strength of the pressure gradient force (8). The first two terms in (8) will be affected. We first consider the extent of this change by setting $\Delta\theta$ equal to a constant value of 6 K in the first of these terms, while retaining the predicted inversion strength in the remainder of the calculations. The result is shown in Fig. 10, with Fig. 5 as the relevant comparison case.

The daytime behavior away from the dryline remains relatively unchanged. The explanation here is that the inversion height is relatively flat during the day, and so the first term in (8) does not play a crucial role in determining the dryline movement. This result disagrees with the shallow-water model results of Miller et al. (2001), where a sinusoidal time variation in the static stability [as measured by the inversion strength (2)] was considered important in moving the dryline eastward during the day. The present results show that in the context of a mixed-layer model, the time variation of static stability plays a minimal role during the day because the height field is so flat.

The situation at night is vastly different. Then the effect of the constant inversion strength in the first term of the pressure gradient force (8) is to increase the surge westward by over 100 km. The change in the surge may be understood by considering the slope of the inversion just after sunset; here it is exceedingly steep and so the term in (8) proportional to the inversion height gradient is large. By keeping $\Delta\theta$ at 6 K for the entire integration, we are making this term at least six times larger in magnitude at sunset than it is when $\Delta\theta$ is allowed to vary ($\Delta\theta \approx 1$ K by sunset in the previous cases). Therefore the pressure gradient produces a greater westward acceleration that drives the dryline farther to the west. This behavior is consistent with the fact that the maximum easterlies are greater in Fig. 10 than those in Fig. 5.

We note that the synoptic pressure gradient force is not included in the calculations leading to the results depicted in Fig. 10. Its inclusion (not shown) has little effect during the day. However, at night the westward surge is much greater than that displayed in Fig. 10 and extends unrealistically westward of $x = -200$ km. Thus the simulations that include the synoptic forcing and predict the inversion strength better simulate the dryline retrogression.

A similar model run to diagnose the role of the pressure gradient term that is proportional to the gradient in the mixed-layer potential temperature [the second term in (8)] was also performed (Fig. 11). This simulation is accomplished by setting this term equal to zero in the integration. The absence of this term had a minimal effect on the movement of the dryline (Fig. 11) and the thermal structure (not shown). However, comparison of Figs. 5 and 11 indicates that the absence of this pressure gradient term has two major effects. First, it produces a zonal wind within 200 km of the dryline that points slightly eastward instead of westward during the day. Second, it leads to a great reduction in the spike in the inversion height at dusk. These effects are interrelated. The thermal gradient term in (8) is directed westward toward warmer air, and because of the increase in potential temperature at the dryline during the day (see section 3a and Figs. 4a and 6a), it acts to drive flow

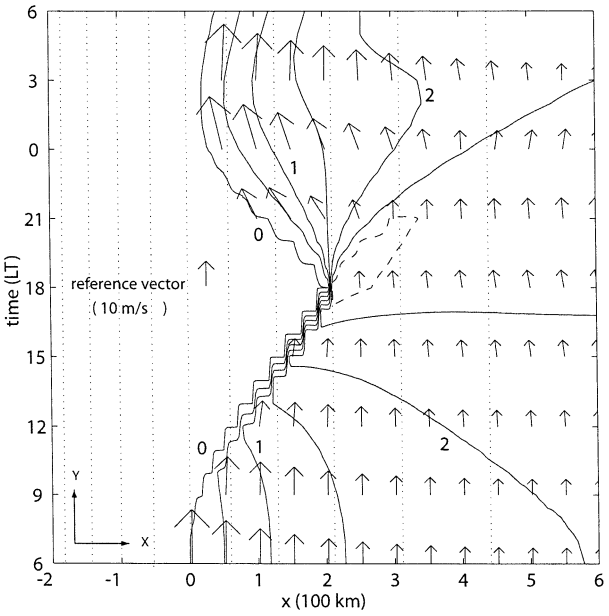

FIG. 11. Contour plot of mixed-layer depth D with wind vectors for the case similar to Fig. 5, but without the pressure gradient term due to the gradient in mixed-layer potential temperature. The dashed contour represents the 2.75-km depth of the mixed layer.

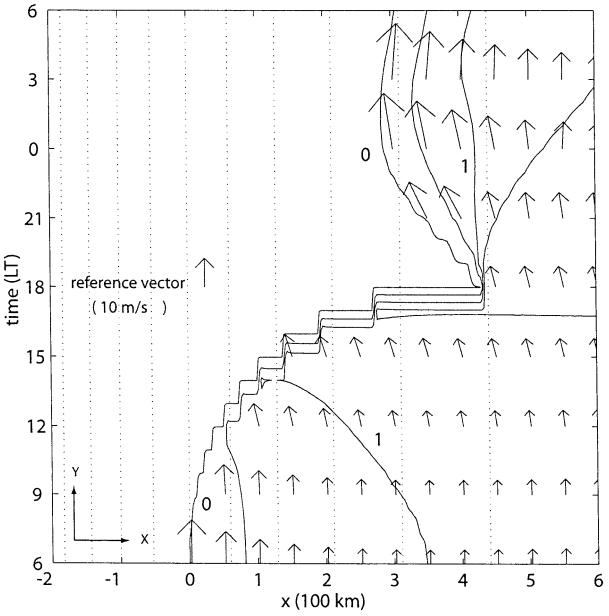

FIG. 12. Contour plot of mixed-layer depth D with wind vectors for the case similar to Fig. 5, but with a far field height $H_0 = 1$ km.

toward the line. This flow is convergent and thus contributes to the production of the spike in the inversion height.

The lack of a significant model response to this term at night agrees with the nocturnal structure of the mixed-layer potential temperature. For example, examination of Fig. 6b shows that the gradient in θ_m is very small from 1800 LT onward.

We next examine the role of the synoptic-scale pressure gradient force [i.e., the third term in (8)]. Model results (not shown) without this term exhibit a slightly larger ($\sim$10 km) eastward movement of the dryline during the day with a similar nocturnal retreat as that displayed in Fig. 5. The major difference is that the maximum low-level jet speed is reduced by 10 m s^{-1}. This result partially supports the view of Blackadar (1957) regarding the evolution of the low-level jet. It also indicates that the movement of the dryline is insensitive to a steady synoptic-scale pressure gradient force.

f. Far field height considerations

We next consider the reduction of the initial far field height to 1 km, or one-half the value it has had up to now. In making such a reduction, we are reducing the total amount of mass contained in the lower layer, and so the inversion should weaken much more easily under this circumstance than before. This behavior can be seen to great effect in Fig. 12, where the eastward movement is approximately 430 km. It is evident that the far field height has a major impact upon the daytime behavior of the dryline. Note the jump in the dryline position is over 100 km from 1700 to 1800 LT. This feature is often observed (e.g., Schaefer 1986) as the discontinuous propagation of the dryline as it leaps eastward. There is no significant effect on the wind field here. The u field reaches 2 m s^{-1} at the dryline by sunset, while the v field there decreases to 7 m s^{-1}. The v field then starts increasing to a maximum of 20 m s^{-1} at 0200 LT, while the u field has a maximum of 8 m s^{-1} toward the west at 2100 LT, before veering to the east.

Inspection of the thermodynamic fields (not shown) indicates that the inversion strength is only a few tenths of a Kelvin by dusk. As a result, almost the entire layer has been eliminated by sunset. This situation arises because we are applying the same amount of heating as before to essentially one-half the mass. So the mixed-layer temperature increases much more, and the inversion strength is correspondingly much weaker than in previous cases. If the heat flux amplitude were much larger than 0.30 K m s^{-1}, the entire mixed layer would have been eliminated by sunset.

The nighttime behavior is not affected qualitatively by the change in far field height. A westward surge of about 150 km is accompanied by an increase in the inversion strength to 4 K by dawn. The surge is slightly decreased over previous simulations. Miller et al. (2001) show that the surge speed is proportional to the gravity wave phase speed c_g. Thus, the reduced surge in this simulation can be explained by noting that $\Delta\theta$ is so small at 1800 LT and that the reduced mixed-layer depth also reduces the gravity wave speed.

g. 3-day integration

Figure 13 shows the result of running our model for a 3-day cycle. The parameter space is identical to that

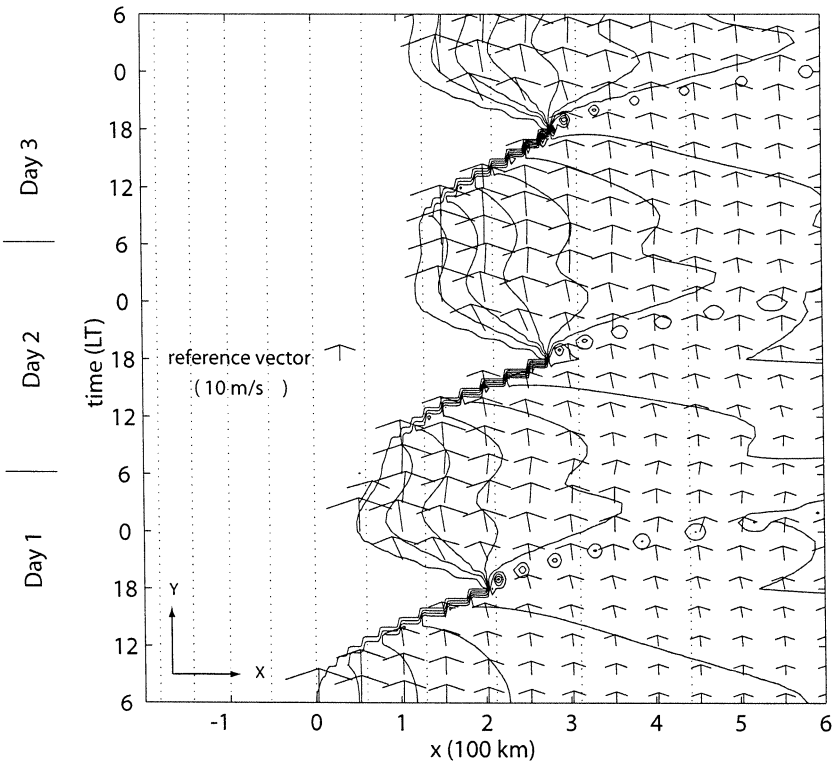

FIG. 13. Contour plot of mixed-layer depth D with wind vectors for the 3-day integration. Full physics included with heating and cooling as in the case for Fig. 5.

for the case in Fig. 5. The movement of the dryline during each individual day is typical of what we have found for each 1-day case presented. The behavior on the third day displays a stabilization because the dryline at dawn ends up where it had started from the previous morning. By this time, the loss of mass at the dryline during the day is balanced by the entrainment of mass into the mixed layer east of the dryline. Because the results for the individual days in the 3-day simulation are so similar, we conclude that the results of the 1-day simulations are not particularly sensitive to the initial conditions. Table 2 summarizes the wind field extrema near the dryline, as well as the thermodynamic far field values. The v-field data clearly indicate nocturnal jets around 0000 LT and 0100 LT, with the westward zonal wind maximizing at 2000 LT to 2100 LT.

The parameter space one uses for a 3-day integration is not as arbitrary as that for a 1-day integration. It is possible, for example, that if the daytime heating is too large, or the nighttime cooling too small, then the inversion strength at 0600 LT of the next day would be too small to accommodate that day's heating. Therefore, a set of values for the heat flux amplitude and nighttime cooling that give acceptable results in a 1-day case may not do so in a 3-day case.

4. Conclusions

The results of the present study are in general agreement both with previous dryline simulations and with observational studies of the Great Plains springtime dryline environment. These include the eastward movement of the dryline and the steepening of the dry front during the day, the westward gradient of the mixed-layer po-

TABLE 2. Extrema of the dynamical and thermodynamical fields for the 3-day integration. Parameter settings are the same as in Fig. 13. Here u- and v-field values are near the leading edge, with $\Delta\theta$ values are for the far field. Time of occurrence (in LT) for each value is indicated in parentheses.

Extrema	Day 1	Day 2	Day 3
u_{min} (m s^{-1})	−2.4 (1800 LT)	−2.0 (1800 LT)	−1.9 (1800 LT)
u_{max} (m s^{-1})	−9.0 (2100 LT)	−9.0 (2000 LT)	−9.2 (2100 LT)
v_{min} (m s^{-1})	9.1 (1800 LT)	10.0 (1800 LT)	11.0 (1800 LT)
v_{max} (m s^{-1})	22.0 (0100 LT)	23.0 (0000 LT)	25.0 (0100 LT)
$\Delta\theta_{min}$ (K)	1.2 (1800 LT)	1.4 (1800 LT)	2.1 (1800 LT)
$\Delta\theta_{max}$ (K)	5.1 (0600 LT)	5.3 (0600 LT)	6.1 (0600 LT)

tential temperature, the inverse effect during the night, and the development of a nocturnal low-level jet. Thus our model supports the hypothesis (Schaefer 1973, 1974a,b; Sun and Wu 1992) that boundary layer heating is sufficient to drive the dryline, and explain its diurnal variation. The model dryline can exhibit discontinuous eastward movement (see section 3f) when the inversion strength is vanishingly small.

A consistent feature in our simulations is the generation of a spike in the inversion height, when the dryline has stopped its eastward advance and started a return to the west. The spike is partly a result of the large entrainment (10) that can occur at the dryline where the inversion strength is small and partly due to the warmward convergent flow driven by the pressure gradient force associated with the westward gradient in the mixed-layer potential temperature (section 3e). Westward flow toward the dryline as it advances eastward is typically observed during the daytime (e.g., Schaefer 1986). It is proposed here that it is this boundary layer convergence just to the east of the dryline that is the mechanism in the atmosphere that breaks the inversion and produces convective activity.

We note that Parsons et al. (2000) observed an elevated bulge in a nocturnal dryline but it appears to propagate toward the dryline rather than away from it as our simulations show. Further research using a two-dimensional mixed-layer model may shed light on this discrepancy.

The present results indicate that the dryline system is particularly sensitive to the amplitude of the surface heat flux relative to the strength of the inversion and the depth of the mixed layer. This sensitivity implies that accurate forecasting of the dryline motion requires detailed knowledge of surface properties (Ziegler et al. 1995) and the ability to predict the cloud cover (McNider and Kopp 1990). This sensitivity also suggests that irregular features of the dryline such as dryline waves and bulges (McCarthy and Koch 1982) may owe their origin to variations in terrain, surface properties, and cloudiness.

Acknowledgments. We thank Christoph Schär for making his shallow-water numerical code available for our use in this study and Jeffrey M. Chagnon and Glenn M. Auslander for programming assistance. The anonymous reviewers made constructive criticisms to the manuscript. The National Science Foundation (NSF) under NSF Grant ATM-9729631 provided partial financial support.

REFERENCES

Blackadar, A. K., 1957: Boundary layer wind maxima and their significance for the growth of nocturnal inversions. *Bull. Amer. Meteor. Soc.*, **38,** 283–290.

Bonner, W. D., 1968: Climatology of the low-level jet. *Mon. Wea. Rev.*, **96,** 833–850.

Keyser, D., and R. A. Anthes, 1977: The applicability of a mixed-layer model of the planetary boundary layer to real-data forecasting. *Mon. Wea. Rev.*, **105,** 1351–1371.

Kovacs, T. A., 1996: Diurnal variation in the movement and structure of the quiescent dryline. M.S. thesis, Department of Meteorology, The Pennsylvania State University, 81 pp.

Lanicci, J. M., and T. T. Warner, 1991: A synoptic climatology of the elevated mixed-layer inversion over the southern Great Plains in spring. Part I: Structure, dynamics, and seasonal evolution. *Wea. Forecasting,* **6,** 181–197.

McCarthy, J., and S. E. Koch, 1982: The evolution of an Oklahoma dryline. Part I: A meso- and subsynoptic scale analysis. *J. Atmos. Sci.,* **39,** 225–236.

McNider, R. T., and F. J. Kopp, 1990: Specification of the scale and magnitude of thermals used to initiate convection in cloud models. *J. Appl. Meteor.,* **29,** 99–104.

Miller, J. A., 1998: A comparison of diurnal motion theories for the quiescent dryline using a shallow water model. M.S. thesis, Department of Meteorology, The Pennsylvania State University, 66 pp.

——, T. A. Kovacs, and P. R. Bannon, 2001: A shallow-water model of the diurnal dryline. *J. Atmos. Sci.,* **58,** 3508–3524.

Parsons, D. B., M. A. Shapiro, and E. Miller, 2000: The mesoscale structure of a nocturnal dryline and of a frontal–dryline merger. *Mon. Wea. Rev.,* **128,** 3824–3838.

Schaefer, J. T., 1973: The motion of the dryline. Preprints, *Eighth Severe Storm Conf.,* Denver, CO, Amer. Meteor. Soc., 104–107.

——, 1974a: A simulative model of dryline motion. *J. Atmos. Sci.,* **31,** 956–964.

——, 1974b: The life cycle of the dryline. *J. Appl. Meteor.,* **13,** 444–449.

——, 1986: The dryline. *Mesoscale Meteorology and Forecasting,* P. S. Ray, Ed., Amer. Meteor. Soc., 549–572.

Schär, C., and R. B. Smith, 1993: Shallow water flow past isolated topography. Part I. Vorticity production and wake formation. *J. Atmos. Sci.,* **50,** 1373–1400.

——, and P. K. Smolarkiewicz, 1996: A synchronous and iterative flux-correction formalism for coupled transport equations. *J. Comput. Phys.,* **128,** 101–120.

Smolarkiewicz, P. K., and L. G. Margolin, 1993: On forward-in-time differencing for fluids: Extension to a curvilinear framework. *Mon. Wea. Rev.,* **121,** 1847–1859.

Stull, R. B., 1988: *An Introduction to Boundary Layer Meteorology.* Kluwer Academic, 666 pp.

Sun, W. Y., and C. C. Wu, 1992: Formation and diurnal variation of the dryline. *J. Atmos. Sci.,* **49,** 1606–1619.

Tennekes, H., 1973: A model for the dynamics of the inversion above a convective boundary layer. *J. Atmos. Sci.,* **30,** 558–567.

Tepper, M., 1955: On the generation of pressure-jump lines by the impulsive addition of momentum to simple current systems. *J. Meteor.,* **12,** 287–297.

Wexler, H., 1961: A boundary layer interpretation of the low-level jet. *Tellus,* **13,** 368–378.

Zeman, O., and H. Tennekes, 1977: Parameterization of the turbulent energy budget at the top of the daytime atmospheric boundary layer. *J. Atmos. Sci.,* **34,** 111–123.

Ziegler, C. L., and C. E. Hane, 1993: An observational study of the dryline. *Mon. Wea. Rev.,* **121,** 1134–1151.

——, W. J. Martin, R. A. Pielke, and R. Z. Walko, 1995: A modeling study of the dryline. *J. Atmos. Sci.,* **52,** 263–285.